

Topological hierarchy in non-Hermitian three-dimensional photonic crystalsYuexin Zhang, Xiaoyu Dai, and Yuanjiang Xiang ^{*}*School of Physics and Electronics, Hunan University, Changsha 410082, China*

(Received 25 April 2024; revised 15 July 2024; accepted 26 August 2024; published 5 September 2024)

The C_n -symmetric topological crystalline insulator (TCI) emerges as a well-established platform known for exhibiting confined edge and corner states protected by spatial rotational symmetry in Hermitian systems. However, the exploration of non-Hermitian photonic TCIs remains relatively underdeveloped. In this study, we introduce a topological hierarchy (TH) within an alternating gain-loss photonic crystal, encompassing non-Hermitian two-dimensional surface, one-dimensional (1D) hinge, and zero-dimensional corner modes. Our methodology demonstrates a complete TH by manipulating vertical and in-plane couplings. Our analysis shows that both the real and imaginary parts of the energy bands maintain symmetry along the zero-energy line, illustrating a TH similar to that observed in Hermitian systems. Study reveals that in the non-Hermitian case, 1D hinge modes are split into two distinct directions with different real and imaginary component wave intensities. Further investigation shows that our design supports a TH and non-Hermitian higher-order topological modes in higher-orbital band gaps. This work expands the study of three-dimensional non-Hermitian photonic systems and offers a promising route to manipulate wave transmission in disentangled higher-orbital bands.

DOI: [10.1103/PhysRevB.110.104103](https://doi.org/10.1103/PhysRevB.110.104103)**I. INTRODUCTION**

The development of topological insulators (TIs) over the past few decades has advanced the field of condensed matter physics [1–3]. TIs are characterized by integer topological invariants—e.g., the Chern number, in momentum space—which exhibit band topology that conforms to bulk-boundary correspondence. Topological crystalline insulators (TCIs), which host hundreds of space groups and spatial symmetries, exhibit bulk dipole moments and support fractionized boundary charge [4–10]. Recently, higher-order topological insulators (HOTIs) have been extensively studied. HOTIs have higher bulk quadrupole moments and fractionized corner modes in two-dimensional (2D) TCIs [11–21]. In three-dimensional (3D) configurations, quadrupole moments contribute to hinge states, while octupole moments give rise to corner-bound charges [22–30]. Efforts have been made concerning 2D TCIs in acoustics, photonics, and nanostructures, where robust in-gap corner modes have been successfully observed [31–33]. Experiments have been carried out to implement TCIs in 3D structures, such as topological quadrupolar semimetals based on rotational symmetry, resulting in localized hinge modes [34–42]. In parallel, 3D photonic TIs reveal other intriguing physical phenomena such as 3D photonic Chern insulators [43–45], 3D dislocations [46], and so on [47–50].

Recently, the concept of topological hierarchy (TH) was proposed to achieve the coexistence of surface, hinge, and corner states within a single model by adjusting both in-plane and out-of-plane couplings [51–53]. The establishment of each hierarchy involves the elimination of band degeneracy. When the one-dimensional (1D) Su-Schrieffer-Heeger (SSH) chain is topological, the 3D bulk mode undergoes splitting into two

components: in-plane bulk modes and out of plane boundary states. By further adjusting the ratio of intra- and intercell coupling terms, the 2D TCI develops in-plane hinge and corner states. To date, the majority of existing THs have been explored in acoustic crystals, mainly due to the easier manipulation of sonic wave wavelengths in experimental settings.

In addition, the phononic lattice structure facilitates air transmission within atom tubelike tunnels and cavities, with a band spectrum that aligns with tight-binding models (TBMs). In contrast, the intricate electromagnetic (EM) properties of photonic crystals (PhCs) pose challenges in designing and fabricating THs on photonic platforms. Similar difficulties arise in the context of 3D photonic crystals. Recently, work on a photonic DH in the Mie-confined resonance framework revealed the possibility of manipulating EM waves at different dimensions [54]. Meanwhile, Mie-confined resonance PhCs have also been shown to be qualified candidates for deriving disentangled higher-orbital band gaps [55]. However, the realization of TH in a non-Hermitian photonic system is rarely discussed.

In this investigation, we present a non-Hermitian PhC consisting of a double-monolayer C_4 -symmetric TCI comprising gain and loss dielectric pillars. To establish vertical couplings, the lattice is covered with drilled metal plates at the top and bottom, effectively forming a one-dimensional SSH chain. The embedded metal pillars in the PhC result in a confined Mie-resonance state, and EM waves are strongly localized around the dielectric cylinders at the lowest bands, matching the linear combination of atomic orbitals in TBMs. We use topological indices to identify the third-order topology of the photonic TCI by analyzing the irreducible representation of rotational invariant points on occupied bands [56]. Simulations show that a nested hierarchy of topological phases is available in our designed frameworks. As the non-Hermitian term continues to grow, the imaginary parts of the higher-order topological phases are well distinguished,

^{*}Contact author: xiangyuanjiang@126.com

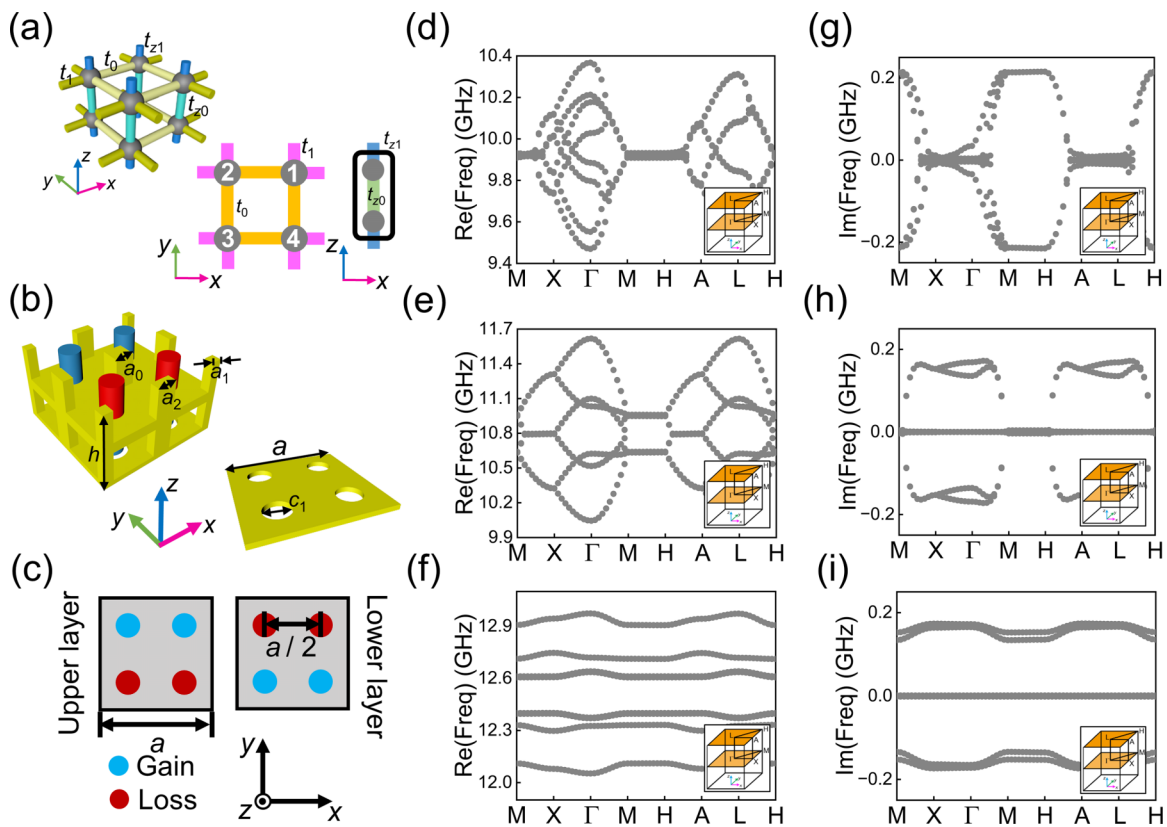


FIG. 1. The schematic presentations of the proposed 3D non-Hermitian PhC and corresponding real and complex band structures. (a) 3D and horizontal and vertical visions of the TBM with C_4 symmetry. (b) The architecture of the unit cell: the blue and red cylinders represent the dielectric rods with gain and loss term. (c) The in-plane schematic view of the upper and lower layers in the PhC. (d)–(f) The real part of the energy bands with equal in-plane and out of plane couplings, nontrivial SSH chain, and both nontrivial in-plane and out of plane couplings. (g)–(i) Imaginary part of the energy bands with $t_1 = t_0$ and $t_{z1} = t_{z0}$, $t_1 = t_0$ and $t_{z1} > t_{z0}$, and $t_1 > t_0$ and $t_{z1} > t_{z0}$.

and the traditional hinge states are separated into vertical and horizontal components. Also, the $|E_z|$ intensity of the hinge with alternating gain-loss array is strongly depressed compared to the hinge with the same gain or loss dielectric rods. Finally, we extend the non-Hermitian higher-order photonic modes to higher-orbital band gaps and prove the existence of robust hinge wave propagation. Our model validates the existence of TH in non-Hermitian photonic systems, establishes the feasibility of this approach for the development of photonic devices capable of engineering EM waves in multiple dimensions, and enriches the story of non-Hermitian physics in higher-orbital bands.

II. CONSTRUCTIONS OF THE 3D PHOTONIC CRYSTAL

To present the full dimensional hierarchy of our photonic TCIs in a straightforward picture, we introduce the minimal TBM of the PhC. The unit cell is divided into two parts: in-plane monolayer lattices and vertical SSH chains. Figure 1(a) conceptually depicts the double-layer Hermitian TCI with C_4 rotational symmetry. The intra- and intercell hopping terms are t_0 and t_1 , while the intra- and interlayer couplings are t_{z0} and t_{z1} . To begin with, we set the gain and loss term as zero to write the Hermitian Hamiltonian of these complete 3D TBM models with C_n rotational symmetry as

$$H(\mathbf{k}) = H_z \otimes I_4 + I_2 \otimes H_{xy}, \quad (1)$$

where I_2 and I_4 are 2×2 and 4×4 identity matrices, respectively. H_{xy} is the Hamiltonian of the in-plane monolayer lattice, and H_z is the Hamiltonian of vertical SSH chains. Here, $H_z = (t_{z0} + t_{z1} \cos k_z) \sigma_x + \sin k_z \sigma_y$ is the vertical SSH Hamiltonian, σ_x and σ_y are Pauli matrices, and the monolayer C_4 -symmetric lattice Hamiltonian $H_{xy} = [0, \mathbf{h}_4(k_x, k_y); \mathbf{h}_4^*(k_x, k_y), 0]$ with $\mathbf{h}_4(k_x, k_y) = [t_0 + t_1 \exp(-ik_x a), t_0 + t_1 \exp(-ik_y a); t_0 + t_1 \exp(ik_x a), t_0 + t_1 \exp(ik_y a)]$. From Eq. (1), we can obtain the eigenenergy of $H(\mathbf{k})$ as $E = E_{xy} + E_z$, and the corresponding eigenstate of the model is expressed as $\Psi = \Psi_{xy} \otimes \Psi_z$. We can describe the dimensional hierarchy of these TCIs as follows: the system keeps bulk modes when Ψ_{xy} and Ψ_z are both bulk states (equal directional couplings with $t_0 = t_1$ and $t_{z0} = t_{z1}$); the model manifests surface states when either of Ψ_{xy} or Ψ_z is nontrivial (altering couplings with $t_0 < t_1$ or $t_{z0} < t_{z1}$); the hinge and corner modes come up when both Ψ_{xy} and Ψ_z remain topological.

In the pursuit of creating a PhC that facilitates both horizontal and vertical transmission of EM waves, a conventional approach is to organize dielectric rods in a lattice configuration. It is imperative to ensure that all resonators maintain an equidistant position from the center of the lattice, while preserving the C_n rotational symmetry [57,58]. Metallic plates are drilled and positioned on the top and bottom of the cylindrical rods, serving as components for vertical couplings.

The hollow circles in the plates and dielectric rods align to ensure equal vertical coupling of resonators in adjacent layers. Metal plates are considered perfect electric conductors (PECs) to prevent interactions between in-plane and out of plane EM wave couplings. Figure 1(b) provides a full 3D view of the C_4 -symmetric PhC. The lattice consists of two layers, each containing four dielectric rods with embedded PECs at the center and sides of the plane.

Recent research demonstrates the use of a confined Mie-resonance PhC, achieved by inserting metal pillars between dielectric rods [55]. The upper and lower drilled plates act as vertical interlayer coupling, while the drilled central layer acts as intralayer coupling. The ratio of vertical coupling strength is adjusted by varying the size of the air holes in the metal plates. By changing the size of the metal rods, in-plane distortions can be modulated to control the decay amplitude of Mie-resonance states. Similarly, by adjusting SSH interconnect couplings, the size of c_1 and c_0 can be increased or decreased. The lattice parameters are defined as follows: the in-plane and out of plane lattice constants are $a = 24$ mm and $h = 16$ mm, the height of the dielectric pillar is $h_r = 6$ mm; the width of the central metal plane is $w = 1$ mm; the diameter of the cylinder scatter is $d = 4$ mm; the diameter of the upper-lower (middle) drilled holes is c_1 (c_0); the side lengths of the side, corner, and central metal rod are a_2 , a_1 , and a_0 , respectively. The relative dielectric permittivity of dielectric rods is $\varepsilon = 9$. The band diagrams in our papers are calculated by COMSOL MULTIPHYSICS.

III. DIMENSIONAL HIERARCHY IN THE NON-HERMITIAN PHOTONIC CRYSTAL

It is natural to ask whether TH can be realized in non-Hermitian systems [59–65]. Recently, a proposal for higher-order non-Hermitian 3D topological PhC was introduced to support topological phase transitions [66]. This is achieved by designing a gain-loss layered SSH model along the z direction and an alternating gain-loss domain wall at the in-plane interface. The system exhibits strongly localized surface, hinge, and corner states. However, this framework includes honeycomb-shaped stacked PhCs with non-Hermiticity only in the vertical direction, leading to the availability of 1D hinge and zero-dimensional (0D) corner states in the presence of layered SSH unit cells with opposite gain-loss placement at each layer. In other words, higher-order topological phases emerge at the interface boundary in a multilayer metasample. In addition, the in-plane distortion is achieved by moving the dielectric rods toward or behind the lattice center, which is relatively inconvenient and suffers from the slow-decaying Mie-resonance states. In our non-Hermitian scheme, as depicted in Fig. 1(b), the gain and loss terms are obtained by defining the signs of the imaginary part (γ) of the relative permittivity. The cylinder placement on the upper and lower layers of the square lattice is opposite, where the red (blue) rods represent loss (gain) with $\gamma = 0.5$ (-0.5). Therefore, we define the relative permittivity of the gain (loss) rods as $9 + 0.5i$ ($9 - 0.5i$), and the lattice incorporates two non-Hermitian SSH chains in both the y and z directions. The Hamiltonian of the non-Hermitian square PhC is

written as

$$H(\mathbf{k}) = H_{\text{NH}}(\mathbf{k}) + \begin{bmatrix} 0 & A^\dagger & B^\dagger & 0 & C & 0 & 0 & 0 \\ A & 0 & 0 & B^\dagger & 0 & C & 0 & 0 \\ B & 0 & 0 & A^\dagger & 0 & 0 & C & 0 \\ 0 & B & A & 0 & 0 & 0 & 0 & C \\ C^\dagger & 0 & 0 & 0 & 0 & A^\dagger & B^\dagger & 0 \\ 0 & C^\dagger & 0 & 0 & A & 0 & 0 & B^\dagger \\ 0 & 0 & C^\dagger & 0 & B & 0 & 0 & A^\dagger \\ 0 & 0 & 0 & C^\dagger & 0 & B & A & 0 \end{bmatrix}, \quad (2)$$

where $A = t_0 + t_1 \exp(ik_x)$, $B = t_0 + t_1 \exp(ik_y)$, $C = t_{z0} + t_{z1} \exp(ik_z)$, and $H_{\text{NH}}(\mathbf{k}) = \text{diagonal} \{i\gamma, i\gamma, -i\gamma, -i\gamma, -i\gamma, -i\gamma, i\gamma, i\gamma\}$, where $i\gamma$ ($-i\gamma$) denotes the on-site loss (gain) for each cylinder of a square unit cell. $H(\mathbf{k})$ preserves the anti-parity-time (PT) symmetry with $(PT)H(\mathbf{k})(PT)^{-1} = -H(\mathbf{k})$; P and T are parity and time operators. The eigenfrequencies of the non-Hermitian band structure are composed of real and complex values compared to the Hermitian system. Figures 1(d)–1(f) gives the real part of the band spectrum of the non-Hermitian square lattice under original ($t_1 = t_0$, $t_{z1} = t_{z0}$), first-order ($t_1 = t_0$, $t_{z1} > t_{z0}$), and second-order ($t_1 > t_0$, $t_{z1} > t_{z0}$) configurations, respectively. The geometrical parameters of the first- and second-order square PhC are the same as the Hermitian system given in the Supplemental Material [67]. It can be found that the band degeneracy collapses as the equal couplings are broken. More importantly, the dimensional hierarchy appears in the imaginary part of the eigenbands, as plotted in Figs. 1(g)–1(i).

Next, we consider the realization of non-Hermitian 2D surface and 1D hinge modes in our square PhC. We construct a three-layer stacked PhC array along the z direction, as shown in Fig. 2(a). The top and bottom of the supercell are covered with undrilled metal plates to produce PEC boundaries. The x and y directions are still periodic conditions. Figures 2(b) and 2(e) show the calculated surface mode profiles $|E_z|$ with the first- and second-order supercells ($t_1 > t_0$, $t_{z1} > t_{z0}$). The corresponding real and complex surface band diagrams of first- and second-order supercells are plotted in Figs. 2(c), 2(d), 2(f), and 2(g), respectively. It is obvious that these energy bands experience the degeneracy lifting process when the system transmits from the first-order TI to the second-order TI. In addition, the projected complex surface bands, Figs. 2(d) and 2(g), are symmetrically located along the zero-energy line. To build a second-order square PhC hosting 1D hinge modes, we expand the surface supercell along the y direction to allow transmission of hinge states along the edge, as depicted in Fig. 2(h). Two ends of the hinge supercell are cut to formulate PEC boundaries in the y direction. In this way, we have a horizontal SSH chain with alternating gain and loss sites along the y direction. Figures 2(j) and 2(k) calculate the corresponding real and complex part of hinge dispersions, where band degeneracy occurs at about 9.64 GHz at $k_x = \pi/a$, and the corresponding hinge eigenmode fields of the hinge supercell are displayed in Fig. 2(i).

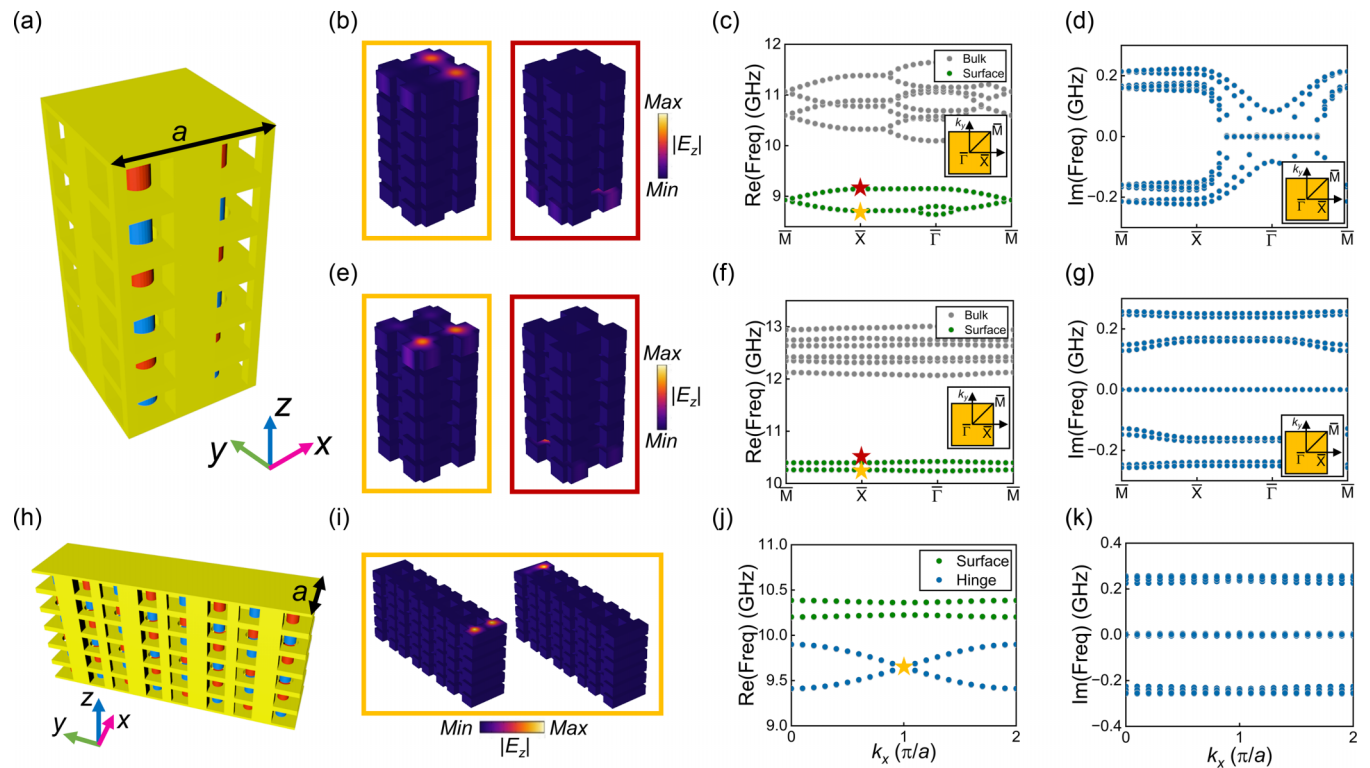


FIG. 2. The non-Hermitian surface and hinge supercell and corresponding real and complex band structures. (a) The architecture of the stacking non-Hermitian square supercell, where the blue and red cylinders represent the dielectric rods with gain and loss, respectively. (b) Normalized electric field distributions of the first-order surface states at $8.71 - 0.21i$ and $9.14 + 0.22i$ GHz, respectively. (c),(d) Real and imaginary parts of the energy bands of the first-order supercell. (e) Normalized electric field distributions of the second-order surface states at $10.26 - 0.24i$ and $10.40 - 0.25i$ GHz, respectively. (f),(g) Real and imaginary parts of the energy bands of the second-order supercell. (h) The 3D view of the non-Hermitian hinge supercell. (i) Normalized electric field distributions of the hinge states at $9.64 + 0.24i$ and $9.64 - 0.24i$ GHz, respectively. (j),(k) Real and imaginary part of the second-order hinge supercell band diagrams.

We investigate eigenmode solutions in a non-Hermitian system using a multilayer PhC array, as illustrated in Fig. 3(a). Each layer consists of 25 unit cells with PEC boundaries at the four edges. Figure 3(d) displays the eigenmode solutions of the stacked sample in a Hermitian system, where eight degenerate corner states (depicted by orange dots) are observed around 9.15 GHz, while the hinge modes (represented by light blue dots) span from 9.42 to 9.88 GHz. Introducing a non-Hermitian term of $\gamma = 0.5$, we observe the distributions of real and imaginary solutions in the multilayer sample, illustrated in Figs. 3(e) and 3(f). Compared to the Hermitian model, the real parts of the eigenmodes with $\gamma = 0.5$ exhibit two distinct types of hinge modes: horizontal (H hinge represented by dark blue dots) and vertical (V hinge represented by light blue dots). Additionally, the imaginary parts of the eigenmode solutions are nonzero.

To provide a clearer understanding of non-Hermitian features, we calculate the PT -symmetry complex phase diagram of corner and hinge states, as depicted in Figs. 3(b) and 3(c). In Fig. 3(b), we illustrate the spectral positions of the second corner state in the eigenmode solutions shown in Figs. 3(d) and 3(e). It is evident that as γ increases, the complex conjugate corner states (corner 1 and corner 2) exhibit a linear tendency to move in opposite directions. When it comes to the hinge phase transition diagram, as pictured in

Fig. 3(c), we find an exceptional point of $i = 0.483$. The two hinge modes maintain the PT -symmetric phase for $i < 0.483$, where the imaginary parts degenerate at zero. If $i > 0.483$, the PT -symmetric phase is broken for the hinge modes, and the imaginary components become a complex conjugate pair. The inset in Fig. 3(c) plots the zoom-in PT -symmetric phase transition point at $i = 0.483$ (marked by the dashed line). It can be noticed that the two hinge eigenmodes (hinge 1 and hinge 2) in Fig. 3(c) are a complex conjugate pair that is closer to the imaginary zero-energy line. Additionally, we plot the transmission fields of hinge electromagnetic (EM) waves for both the Hermitian and non-Hermitian ($\gamma = 0.5$) cases. Figure 3(g) displays the hinge eigenmodes at 9.46 and 9.84 GHz, where the hinge state propagates along the top sides of the stacked sample. Figure 3(h) shows V-hinge eigenmodes at $9.64 + 0.23i$ and $9.84 + 0.63i$ GHz, while Fig. 3(i) illustrates H-hinge eigenmodes at $9.46 - 0.23i$ and $9.46 + 0.23i$ GHz. The introduction of the non-Hermitian parameter γ divides the original hinge modes into two orthogonal components.

IV. INFLUENCE OF THE NON-HERMITICITY ON HIGHER-ORDER HINGE MODES

We conduct a detailed analysis of the transmission properties of the non-Hermitian H-hinge and V-hinge states as γ varies. To excite surface wave propagation, a source (red

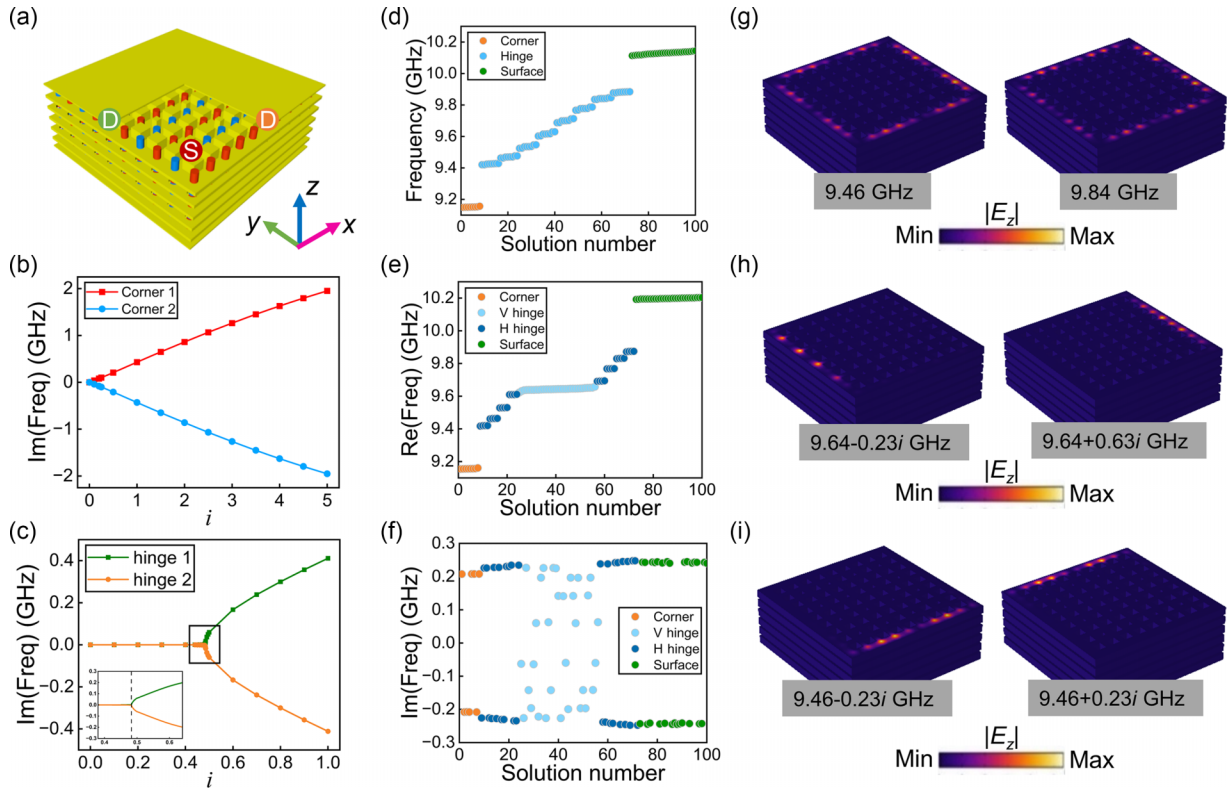


FIG. 3. The construction of 3D PhC with six layers and corresponding eigenmode solutions, and electric field distributions. (a) The 3D view of the non-Hermitian stacking TCI model composed of second-order square PhCs. The part of the top metal plane is deleted for the visualization of gain and loss cylinders at each layer. (b),(c) PT -symmetry complex phase diagram of the corner and hinge states. (d) Solution numbers of the Hermitian multilayer 3D PhC. (e),(f) Real and imaginary part of the solution numbers of the non-Hermitian sample with $\gamma = 0.5$. (g) Normalized electric field distributions of the Hermitian model. (h),(i) Normalized electric field distributions of the non-Hermitian model.

circle) is placed on top of the stacked sample consisting of alternating gain and loss cylinder resonators, as illustrated in Fig. 3(a). Two detectors positioned on the vertical and horizontal top sides (green circle and orange circle) are deployed to measure the intensity profiles of V-hinge and H-hinge EM waves. We extract the real and complex parts of the EM wave intensity spectra under different non-Hermitian parameters $\gamma = 0.05, 0.1, 0.2$, and 0.5 , respectively. Figures 4(a) and 4(e) illustrate the real $[\text{Re}(|E_z|)]$ and imaginary $[\text{Im}(|E_z|)]$ components of $|E_z|$ across the frequency range of 8.5–10.5 GHz with $\gamma = 0.05$. It is evident that the $[\text{Re}(|E_z|)]$ of both the H hinge (orange) and the V hinge (green) within the frequency band of 9.55–9.75 GHz remains approximately constant at magnitudes around 4×10^7 and 5×10^7 V/m. At 9.6 GHz, the $\text{Im}(|E_z|)$ of the V hinge (blue) is almost twice as large as that of the H hinge (yellow). Figure 4(i) presents the normalized EM wave transmission field of the top surface of the multilayer sample with $\gamma = 0.05$ at 9.6 GHz, highlighting the propagation suppression of the H hinge in contrast to the V hinge.

By adjusting $\gamma = 0.1$, the ratio of $\text{Re}(|E_z|)$ between the V hinge and the H hinge reaches 2.7 at 9.65 GHz, as depicted in Fig. 4(b). However, in Fig. 4(f), the $\text{Im}(|E_z|)$ value of the V hinge is 1.25×10^9 V/m, almost 17 times that of the H hinge which measures 7.4×10^7 V/m. Figure 4(j) illustrates the normalized EM wave field distributions of the top slice with $\gamma = 0.1$ at 9.65 GHz, where only the V-hinge mode is

observable. As γ goes to 0.2, the peak value of $\text{Re}(|E_z|)$ for the V hinge (H hinge) reaches 6.8×10^7 V/m (4.3×10^7 V/m) at 9.60 GHz, and the $\text{Im}(|E_z|)$ for the V hinge (H-hinge) measures 1.05×10^7 V/m (5.5×10^7 V/m) at 9.50 GHz (9.55 GHz), as shown in Figs. 4(c) and 4(g). Similarly, Fig. 4(k) shows that only the V-hinge mode is supported on the top surface side at 9.50 GHz.

When $\gamma = 0.5$, the $\text{Re}(|E_z|)$ ratio of the V hinge (H hinge) is 130 at 9.65 GHz, while the $\text{Im}(|E_z|)$ ratio of the V hinge (H hinge) is 2400 at 9.65 GHz, as shown in Figs. 4(d) and 4(h). The surface EM wave transmission graph at 9.65 GHz in Fig. 4(l) shows that only V-hinge mode exists. From these data, it is evident that introducing the non-Hermitian parameter not only introduces non-Hermitian electromagnetic wave components, but also alters the propagation mode of hinge waves. Furthermore, by increasing the magnitude of the non-Hermitian term γ , both the real and imaginary parts of $|E_z|$ for the H-hinge mode are significantly lessened. This implies that the non-Hermitian term can be effectively utilized to adjust the intensity of specific hinge modes as desired.

V. NON-HERMITIAN TH AND HINGE MODES IN HIGHER-ORBITAL BAND GAPS

So far, we have discussed the non-Hermitian topological phase and TH in the lowest band gaps. The higher-order states

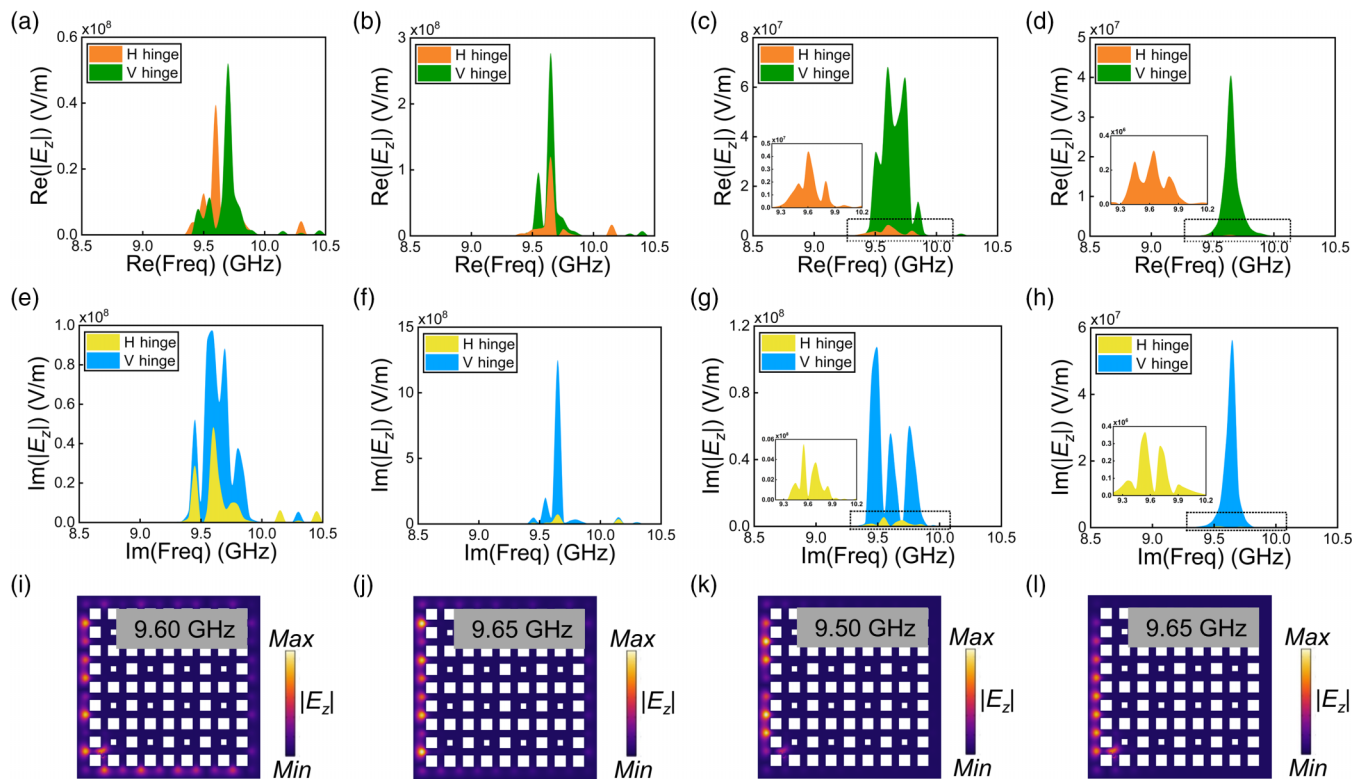


FIG. 4. The real and complex EM wave intensity spectra at different non-Hermitian terms and corresponding hinge wave propagation profiles. (a)–(d) The real components of the H-hinge and V-hinge wave intensity spectra with $\gamma = 0.05, 0.1, 0.2,$ and $0.5,$ respectively. (e)–(h) The imaginary components of the H-hinge and V-hinge wave intensity spectra with $\gamma = 0.05, 0.1, 0.2,$ and $0.5,$ respectively. (i)–(l) The normalized $|E_z|$ propagation field distributions with $\gamma = 0.05, 0.1, 0.2,$ and 0.5 at $9.60, 9.65, 9.50,$ and 9.65 GHz, respectively.

and TH in higher-orbital energy bands are not yet realized in the 3D photonic system. The main difficulty of obtaining a higher-orbital topological phase is the mixed band spectrum in the dielectric PhC. The proposed confined Mie-resonance photonic lattice has successfully make the higher-orbital band gaps disentangled [55]. Inspired by this, we do further study on the non-Hermitian higher-order higher-orbital topological phase in a 3D photonic framework. Figures 5(a)–5(c) [Figs. 5(d)–5(f)] show the real (imaginary) component of higher-orbital band structures under original, first-order, and second-order unit cells, respectively. It is evident that both the real and complex parts of the higher-orbital band spectra behave as a dimensional hierarchy as the directional equal couplings are broken. Similarly, we calculate the projected real and imaginary surface band diagrams of the first- and second-order supercells, as presented in Figs. 5(g) and 5(h) [Figs. 5(j) and 5(k)]. As the supercell experiences a phase shift from the first order to the second order, the surface energy bands will lose the degeneracy properties. Further, we give the hinge supercell band dispersions, as displayed in Figs. 5(i) and 5(l). The hinge states exist in the band gaps from 17.3 to 18.6 GHz, and from 18.7 to 18.9 GHz, matching the band gaps in the second-order surface bands shown in Fig. 5(h).

To prove the existence of the higher-orbital hinge modes in a 3D PhC model, we compute the real and complex solution numbers of the eigenmodes ranging from 17.5 to 19.5 GHz, as shown in Figs. 6(a) and 6(b). The multilayer 3D photonic architecture uses the same settings in Fig. 3(a). We find that the hinge modes are located in the two band gaps of

17.5 – 18.6 GHz and 18.7 – 18.9 GHz, and the imaginary parts of the hinge modes have nonzero values. Finally, we examine the wave transmission of the hinge states in the higher-orbital band gaps by placing two detectors on the top vertical and horizontal edges, as marked in Fig. 3(a). Figures 6(c) and 6(d) provide the $\text{Re}(|E_z|)$ and $\text{Im}(|E_z|)$ intensity profiles of the V hinge and H hinge with non-Hermitian term $\gamma = 0.5$. It can be obviously witnessed that the $\text{Re}(|E_z|)$ of the V hinge (H hinge) is 4×10^9 V/m (1×10^7 V/m) at 18.65 GHz, while the $\text{Im}(|E_z|)$ of the V hinge (H hinge) is 1.25×10^8 V/m (2.7×10^6 V/m) at 18.0 GHz. Figure 6(e) demonstrates the top surface hinge wave propagation field distributions at 18.65 GHz, where only the V hinge is visible, proving the robust higher-orbital hinge wave transmission.

VI. CONCLUSIONS

We establish a non-Hermitian dimensional hierarchy in a 3D square lattice by implementing an alternating loss-and-gain configuration in both the y and z directions. By modulating in-plane and vertical hopping, we successfully induce first-order surface, second-order hinge, and third-order corner states on both the top and bottom surfaces of the 3D samples. Band structures reveal a hierarchy of band degeneracy in both the real and imaginary parts. Our framework supports robust non-Hermitian hinge and corner modes at sample edges without the need to build domain walls. Analysis shows non-Hermitian phase transitions as the parameter increases for both hinge and corner

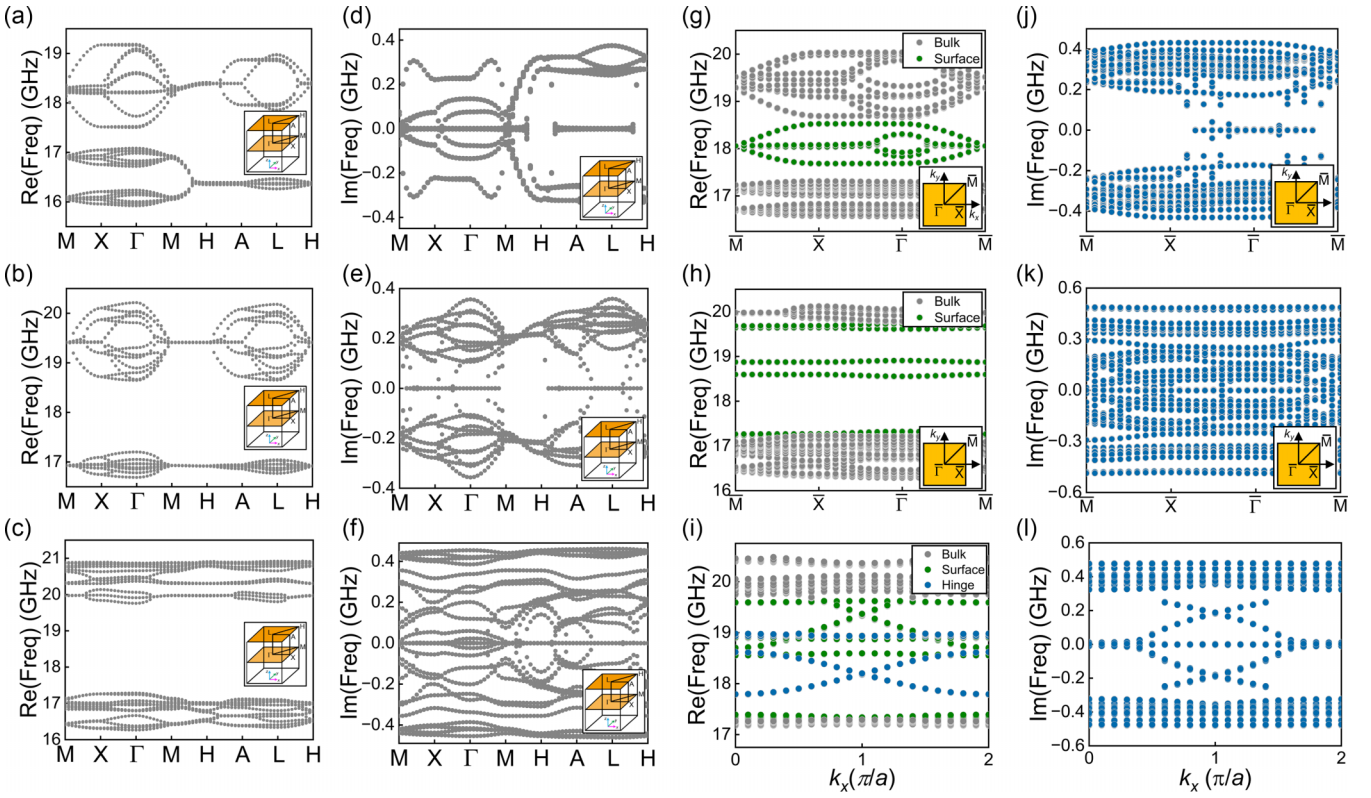


FIG. 5. The real and complex band structures of a square lattice with different dimensional hierarchy. (a)–(c) Real part of band diagrams of original, first-order, and second-order unit cells at higher bands. (d)–(f) Imaginary part of band diagrams of original, first-order, and second-order unit cells at higher bands. (g),(h) Real part of surface band spectra with first- and second-order supercells. (i) Real part of hinge band spectra. (j),(k) Complex part of surface band spectra with first- and second-order supercells. (l) Complex part of hinge band spectra.

modes. In addition, the transmission intensity of both H-hinge and V-hinge modes can be modulated by adjusting the non-Hermitian parameter, resulting in suppression of electromagnetic waves in both real and complex components along orthogonal directions. Further analysis proves that the higher-orbital non-Hermitian higher-order hinge state is also

available in our confined Mie-resonance PhCs. This work opens up possibilities for manipulating optical devices with flexible EM wave engineering at varying dimensions, and paves the way for achieving non-Hermitian higher-order topological phases in higher-orbital bands with exotic physical properties.

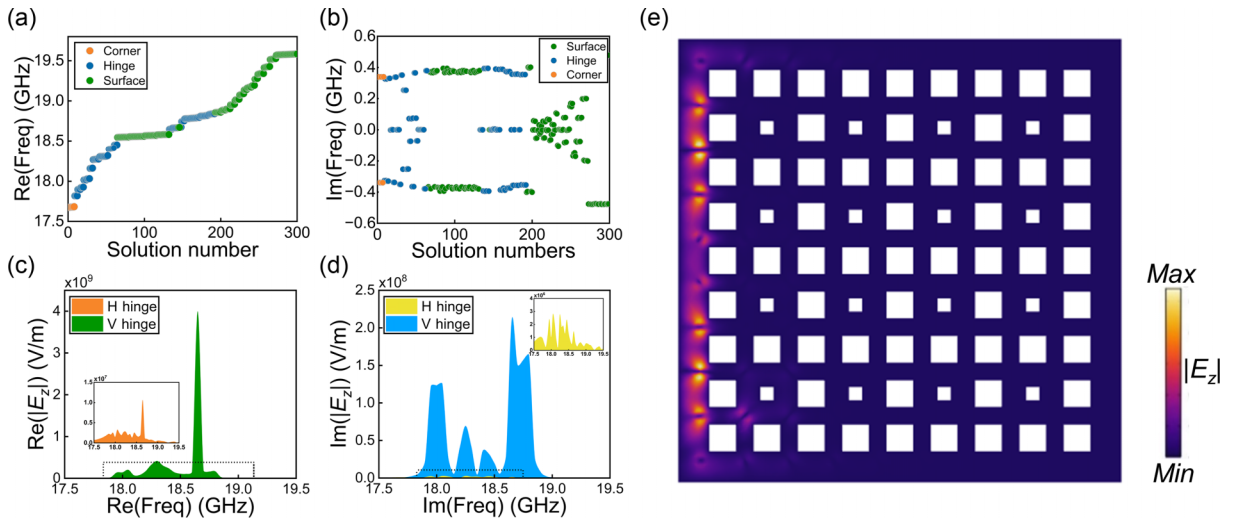


FIG. 6. The real and complex higher-orbital topological phase eigenmode solutions and corresponding hinge wave intensity spectra and propagation profiles. (a),(b) The real and complex components of the eigenmode solutions. (c),(d) The real and imaginary components of the H-hinge and V-hinge wave intensity spectra with $\gamma = 0.5$. The normalized $|E_z|$ higher-orbital hinge propagation field distributions with $\gamma = 0.5$.

ACKNOWLEDGMENTS

This work is partly supported by the National Natural Science Foundation of China (Grant No.

12374302), and the Guangdong Basic and Applied Basic Research Foundation (Grants No. 2023A1515011766 and No. 2023A1515011182).

-
- [1] K. v. Klitzing, G. Dorda, and M. Pepper, New method for high-accuracy determination of the fine-structure constant based on quantized Hall resistance, *Phys. Rev. Lett.* **45**, 494 (1980).
- [2] M. Z. Hasan and C. L. Kane, Colloquium: Topological insulators, *Rev. Mod. Phys.* **82**, 3045 (2010).
- [3] L. Fu, C. L. Kane, and E. J. Mele, Topological insulators in three dimensions, *Phys. Rev. Lett.* **98**, 106803 (2007).
- [4] L. Fu, Topological crystalline insulators, *Phys. Rev. Lett.* **106**, 106802 (2011).
- [5] T. H. Hsieh, H. Lin, J. Liu, W. Duan, A. Bansil, and L. Fu, Topological crystalline insulators in the SnTe material class, *Nat. Commun.* **3**, 982 (2012).
- [6] C. Fang and L. Fu, New classes of three-dimensional topological crystalline insulators: Nonsymmorphic and magnetic, *Phys. Rev. B* **91**, 161105(R) (2015).
- [7] H. Watanabe and L. Fu, Topological crystalline magnets: Symmetry-protected topological phases of fermions, *Phys. Rev. B* **95**, 081107(R) (2017).
- [8] C. Fang and L. Fu, New classes of topological crystalline insulators having surface rotation anomaly, *Sci. Adv.* **5**, eaat2374 (2019).
- [9] W. A. Benalcazar, T. Li, and T. L. Hughes, Quantization of fractional corner charge in C_n -symmetric higher-order topological crystalline insulators, *Phys. Rev. B*, **99** 245151 (2019).
- [10] H. Kondo and Y. Akagi, Dirac surface states in magnonic analogs of topological crystalline insulators, *Phys. Rev. Lett.* **127**, 177201 (2021).
- [11] W. A. Benalcazar, B. A. Bernevig, and T. L. Hughes, Quantized electric multipole insulators, *Science* **357**, 61 (2017).
- [12] W. A. Benalcazar, B. A. Bernevig, and T. L. Hughes, Electric multipole moments, topological multipole moment pumping, and chiral hinge states in crystalline insulators, *Phys. Rev. B* **96**, 245115 (2017).
- [13] B.-Y. Xie, H.-F. Wang, H.-X. Wang, X.-Y. Zhu, J.-H. Jiang, M.-H. Lu, and Y.-F. Chen, Second-order photonic topological insulator with corner states, *Phys. Rev. B* **98**, 205147 (2018).
- [14] F. Liu and K. Wakabayashi, Novel topological phase with a zero Berry curvature, *Phys. Rev. Lett.* **118**, 076803 (2017).
- [15] Z. Song, Z. Fang, and C. Fang, $(d - 2)$ -Dimensional edge states of rotation symmetry protected topological states, *Phys. Rev. Lett.* **119**, 246402 (2017).
- [16] B.-Y. Xie, H.-X. Wang, X.-J. Zhang, P. Zhan, J.-H. Jiang, M.-H. Lu, and Y.-F. Chen, Higher-order band topology, *Nat. Rev. Phys.* **3**, 520 (2021).
- [17] S. Mittal, V. V. Orre, G.-Y. Zhu, M. A. Gorlach, A. Poddubny, and M. Hafezi, Photonic quadrupole topological phases, *Nat. Photonics* **13**, 692 (2019).
- [18] J.-C. Bao, D.-Y. Zou, W.-X. Zhang, W.-J. He, H.-J. Sun, and X.-D. Zhang, Topoelectrical circuit octupole insulator with topologically protected corner states, *Phys. Rev. B* **100**, 201406(R) (2019).
- [19] M. S. Garcia, V. Peri, R. Süssstrunk, O. R. Bilal, T. Larsen, L. G. Villanueva, and S. D. Huber, Observation of a phononic quadrupole topological insulator, *Nature (London)* **555**, 342 (2018).
- [20] M.-Y. Li, D. Zhirihin, M. Gorlach, X. Ni, D. Filonov, A. Slobozhanyuk, A. Alù, and A. B. Khanikaev, Higher-order topological states in photonic kagome crystals with long-range interactions, *Nat. Photonics* **14**, 89 (2020).
- [21] D. A. Bobylev, D. I. Tikhonenko, D. V. Zhirihin, M. Mazanov, A. Vakulenko, D. A. Smirnova, A. B. Khanikaev, and M. A. Gorlach, Topological edge and corner states designed via meta-atoms orientation, *Laser Photonics Rev.* **17**, 2100567 (2023).
- [22] M. Lin and T. L. Hughes, Topological quadrupolar semimetals, *Phys. Rev. B* **98**, 241103(R) (2018).
- [23] X. Ni, M. Li, M. Weiner, A. Alù, and A. B. Khanikaev, Demonstration of a quantized acoustic octupole topological insulator, *Nat. Commun.* **11**, 2108 (2020).
- [24] S. A. A. Ghorashi, T. Li, and T. L. Hughes, Higher-order Weyl semimetals, *Phys. Rev. Lett.* **125**, 266804 (2020).
- [25] H. Xue, Y. Ge, H.-X. Sun, Q. Wang, D. Jia, Y.-J. Guan, S.-Q. Yuan, Y. Chong, and B.-L. Zhang, Observation of an acoustic octupole topological insulator, *Nat. Commun.* **11**, 2442 (2020).
- [26] S. Liu, S. Ma, Q. Zhang, L. Zhang, C. Yang, O. You, W. Gao, Y. Xiang, T. Cui, and S. Zhang, Octupole corner state in a three-dimensional topological circuit, *Light: Sci. Appl.* **9**, 145 (2020).
- [27] A. K. Ghosh, T. Nag, and A. Saha, Dynamical construction of quadrupolar and octupolar topological superconductors, *Phys. Rev. B* **105**, 155406 (2022).
- [28] Z.-X. Li, Z. Wang, Z. Zhang, Y. Cao, and P. Yan, Third-order topological insulator in three-dimensional lattice of magnetic vortices, *Phys. Rev. B* **103**, 214442 (2021).
- [29] Y. Zhang, J. Tang, X. Dai, S. Zhang, Z. Cao, and Y. Xiang, Design of a higher-order nodal-line semimetal in a spring-shaped acoustic topological crystal, *Phys. Rev. B* **106**, 184101 (2022).
- [30] Y.-X. Zhang, J. Tang, X.-Y. Dai, S. Zhang, and Y.-J. Xiang, Higher-order nodal ring photonic semimetal, *Opt. Lett.* **47**, 5885 (2022).
- [31] Y. Ota, F. Liu, R. Katsumi, K. Watanabe, K. Wakabayashi, Y. Arakawa, and S. Iwamoto, Photonic crystal nanocavity based on a topological corner state, *Optica* **6**, 786 (2019).
- [32] L. Zhang, Y.-H. Yang, Z.-K. Lin, P.-F. Qin, Q.-L. Chen, F. Gao, E.-P. Li, J.-H. Jiang, B.-L. Zhang, and H.-S. Chen, Higher-order topological states in surface-wave photonic crystals, *Adv. Sci.* **7**, 1902724 (2020).
- [33] X. Zhang, H. Wang, Z. Lin, Y. Tian, B. Xie, M. Lu, Y. Chen, and J. Jiang, Second-order topology and multidimensional topological transitions in sonic crystals, *Nat. Phys.* **15**, 582 (2019).
- [34] Y. Pan, C. Cui, Q. Chen, F. Chen, L. Zhang, Y. Ren, N. Han, W. Li, X. Li, Z. Yu, H. Chen, and Y. Yang, Real higher-order Weyl photonic crystal, *Nat. Commun.* **14**, 6636 (2023).

- [35] Z. Pu, H. He, L. Luo, Q. Ma, L. Ye, M. Ke, and Z. Liu, Acoustic higher-order Weyl semimetal with bound hinge states in the continuum, *Phys. Rev. Lett.* **130**, 116103 (2023).
- [36] X. Ni, M. Weiner, A. Alù, and A. B. Khanikaev, Robust zero-energy modes in an electronic higher-order topological insulator, *Nat. Mater.* **18**, 113 (2019).
- [37] H.-X. Wang, Z.-K. Lin, B. Jiang, G.-Y. Guo, and J.-H. Jiang, Higher-order Weyl semimetals, *Phys. Rev. Lett.* **125**, 146401 (2020).
- [38] Q. Wei, X.-W. Zhang, W.-Y. Deng, J.-Y. Lu, X.-Q. Huang, M. Yan, G. Chen, Z.-Y. Liu, and S.-T. Jia, *Nat. Mater.* **20**, 812, (2021).
- [39] H.-H. Qiu, M. Xiao, F. Zhang, and C.-Y. Qiu, Higher-order topological semimetal in acoustic crystals, *Phys. Rev. Lett.* **127**, 146601 (2021).
- [40] Z.-H. Wang, D.-J. Liu, H.-T. Teo, Q. Wang, H.-R. Xue, and B.-L. Zhang, Higher-order Dirac semimetal in a photonic crystal, *Phys. Rev. B* **105**, L060101 (2022).
- [41] L. Luo, H.-X. Wang, Z.-K. Lin, B. Jiang, Y. Wu, F. Li, and J.-H. Jiang, Observation of a phononic higher-order Weyl semimetal, *Nat. Mater.* **20**, 794 (2021).
- [42] L. Song, H. Yang, Y. Cao, and P. Yan, Square-root higher-order Weyl semimetals, *Nat. Commun.* **13**, 5601 (2022).
- [43] G. Liu, Z. Gao, Q. Wang, X. Xi, Y. Hu, M. Wang, C. Liu, X. Lin, L. Deng, S. A. Yang, P. Zhou, Y. Yang, Y. Chong, and B. Zhang, Topological Chern vectors in three-dimensional photonic crystals, *Nature (London)* **609**, 925 (2022).
- [44] C. Devescovi, M. G. Díez, I. Robredo, M. B. Paz, J. L. Alonso, B. Bradlyn, J. L. Mañes, M. G. Vergniory, and A. G. Etxarri, Cubic 3D Chern photonic insulators with orientable large Chern vectors, *Nat. Commun.* **12**, 7330 (2021).
- [45] C. Devescovi, M. G. Díez, B. Bradlyn, J. L. Mañes, M. G. Vergniory, and A. G. Etxarri, Vectorial bulk-boundary correspondence for 3D photonic Chern insulators, *Adv. Opt. Mater.* **10**, 2200475 (2022).
- [46] E. Lustig, L. J. Maczewsky, J. Beck, T. Biesenthal, M. Heinrich, Z. Yang, Y. Plotnik, A. Szameit, and M. Segev, Photonic topological insulator induced by a dislocation in three dimensions, *Nature (London)* **609**, 931 (2022).
- [47] S. Kim, T. Christensen, S. G. Johnson, and M. Soljačić, Automated discovery and optimization of 3D topological photonic crystals, *ACS Photonics* **10**, 861 (2023).
- [48] C. Devescovi, A. Morales-Pérez, Y. Hwang, M. García-Díez, I. Robredo, J. L. Mañes, B. Bradlyn, A. García-Etxarri, and M. G. Vergniory, Axion topology in photonic crystal domain walls, *Nat. Commun.* **15**, 6814 (2024).
- [49] Z. Lan, M. L. N. Chen, F. Gao, S. Zhang, and W. E. I. Sha, A brief review of topological photonics in one, two, and three dimensions, *Rev. Phys.* **9**, 100076 (2022).
- [50] Y. Yang, Z. Gao, H. Xue, L. Zhang, M. He, Z. Yang, R. Singh, Y. Chong, B. Zhang, and H. Chen, Realization of a three-dimensional photonic topological insulator, *Nature (London)* **565**, 622 (2019).
- [51] L.-Y. Zheng and J. Christensen, Dirac hierarchy in acoustic topological insulators, *Phys. Rev. Lett.* **127**, 156401 (2021).
- [52] L. Yang, Y. Wang, Y. Meng, Z. Zhu, X. Xi, B. Yan, S. Lin, J. Chen, B.-J. Shi, Y. Ge, S.-Q. Yuan, H. Chen, H.-X. Sun, G.-G. Liu, Y. Yang, and Z. Gao, Observation of Dirac hierarchy in three-dimensional acoustic topological insulators, *Phys. Rev. Lett.* **129**, 125502 (2022).
- [53] Y. Zhang, J. Tang, X. Dai, and Y. Xiang, Flexible dimensional hierarchy of higher-order topology in the stacked kagome-chain acoustic crystal, *Commun. Phys.* **6**, 130 (2023).
- [54] Y. Zhang, X. Dai, and Y. Xiang, Dirac hierarchy in confined Mie resonance photonic crystals, *Phys. Rev. B* **109**, 064105 (2024).
- [55] J. Li, H. Wang, S. Jia, P. Zhan, M. Lu, Z. Wang, Y. Chen, and B.-Y. Xie, Disentangled higher-orbital bands and chiral symmetric topology in confined Mie resonance photonic crystals, *Laser. Photonics Rev.* **18**, 2300543 (2023).
- [56] Y. Liu, S.-W. Leung, F.-F. Li, Z.-K. Lin, X.-F. Tao, Y. Poo, and J.-H. Jiang, Bulk-disclination correspondence in topological crystalline insulators, *Nature (London)* **589**, 381 (2021).
- [57] B.-Y. Xie, G.-X. Su, H.-F. Wang, H. Su, X.-P. Shen, P. Zhan, M.-H. Lu, Z.-L. Wang, and Y.-F. Chen, Visualization of higher-order topological insulating phases in two-dimensional dielectric photonic crystals, *Phys. Rev. Lett.* **122**, 233903 (2019).
- [58] X.-D. Chen, W.-M. Deng, F.-L. Shi, F.-L. Zhao, M. Chen, and J.-W. Dong, Direct observation of corner states in second-order topological photonic crystal slabs, *Phys. Rev. Lett.* **122**, 233902 (2019).
- [59] Z. Zhang, M. Rosendo López, Y. Cheng, X. Liu, and J. Christensen, Non-Hermitian sonic second-order topological insulator, *Phys. Rev. Lett.* **122**, 195501 (2019).
- [60] L. J. Maczewsky, M. Heinrich, M. Kremer, S. K. Ivanov, M. Ehrhardt, F. Martinez, Y. V. Kartashov, V. V. Konotop, L. Torner, D. Bauer, and A. Szameit, Nonlinearity-induced photonic topological insulator, *Science* **370**, 701 (2020).
- [61] X. Cheng, C. Jouvaud, X. Ni, S. H. Mousavi, A. Z. Genack, and A. B. Khanikaev, Robust reconfigurable electromagnetic pathways within a photonic topological insulator, *Nat. Mater.* **15**, 542 (2016).
- [62] J. Jiang, B. Yan, Y. Peng, J. Xie, A. Shi, and J. Liu, Multiband topological states in non-Hermitian photonic crystals, *Opt. Lett.* **47**, 437 (2022).
- [63] H. Gao, H. R. Xue, Z. M. Gu, T. Liu, J. Zhu, and B. L. Zhang, Non-Hermitian route to higher-order topology in an acoustic crystal, *Nat. Commun.* **12**, 1888 (2021).
- [64] H. Fan, H. Gao, T. Liu, S. An, X. Kong, G. Xu, J. Zhu, C.-W. Qiu, and Z. Su, Reconfigurable topological modes in acoustic non-Hermitian crystals, *Phys. Rev. B* **107**, L201108 (2023).
- [65] X. W. Luo and C. W. Zhang, Higher-order topological corner states induced by gain and loss, *Phys. Rev. Lett.* **123**, 073601 (2019).
- [66] X. Wang, R. Gu, Y. Li, H. Qi, X. Hu, and Q. Gong, Higher-order states in a non-Hermitian 3D topological photonic crystal, *Laser Photonics Rev.* **18**, 2300204 (2024).
- [67] See Supplemental Material at <http://link.aps.org/supplemental/10.1103/PhysRevB.110.104103> for topological invariant index to measure higher-order properties, the band inversion properties of the C_4 -symmetric lattice with first-order hierarchy, the topological invariant index to measure higher-order properties in a non-Hermitian system, and the band inversion properties of the non-Hermitian square lattice with first-order hierarchy.